Supporting Information for:

Spin Dynamics in Ru^{III}-Oxalate Complexes: Synthesis, Characterization, and Ab Initio Insights

Federico Mesa,[a] Carolina Pacheco,[a] Javier González–Platas,[b] Carlos Cruz,[c] Verónica Paredes–García,[c,d] Nicolás Veiga,[a] Lorena Martínez[a] and Raúl Chiozzone*[a]

a) Universidad de la República, Facultad de Química, Área Química Inorgánica, Montevideo, Uruguay.
b) Universidad de La Laguna, Departamento de Física, Instituto Universitario de Estudios Avanzados en Física Atómica, Molecular y Fotónica (IUDEA), MALTA Consolider Team, La Laguna, Tenerife, Spain.
c) Center for the Development of Nanoscience and Nanotechnology, CEDENNA, Santiago de Chile, Chile.
d) Universidad Andrés Bello, Facultad de Ciencias Exactas, Departamento de Ciencias Químicas, Santiago de Chile, Chile.

* Corresponding author: rchiozzo@fq.edu.uy

Experimental

Materials and methods.

Reagents and solvents were purchased from commercial sources and used as received. Ruthenium(III) chloride hydrate ($RuCl_3 \cdot xH_2O$, $x \approx 3$, Oakwood Chemical) was stored in a desiccator containing P_2O_5 for a minimum of 24 hours prior to use. Infrared spectra were recorded with a Shimadzu Prestige 21 FTIR spectrophotometer as KBr pellets in the 4000-400 cm^{-1} region. UV-vis spectra were measured in dmf solution with a Shimadzu UV-1900 using a 1.0 cm quartz cell. Elemental analyses (C, H and N) were performed by using a Thermo Scientific model Flash 2000 elemental analyser.

Synthetic procedures.

Synthesis of $(PPh_4)_2(H_3O)[RuCl_2(ox)_2]\cdot 4H_2O$ ($1\cdot 4H_2O$). A mixture of ruthenium(III) chloride hydrate (100 mg, ca. 0.48 mmol), oxalic acid dihydrate (100 mg, 0.72 mmol) and potassium oxalate monohydrate (135 mg, 0.72 mmol) in water (2 mL) was heated at 130 °C for 1.5 hours in a microwave reactor Anton Paar Monowave 200. The resulting orange solution was allowed to cool to room temperature, acidified with a few drops of concentrated hydrochloric acid (pH < 1) and PPh_4Cl (550 mg, 1.44 mmol) dissolved in the minimum volume of water was added. A small amount of precipitated powder was filtered and discarded, and the filtrate was maintained at room temperature for one week to give large prismatic orange crystals. These were collected by vacuum filtration, washed with several portions of cold water and dried first in air, and then in vacuo over silica gel for two days. Yield: 60 % (260 mg). Dried solid analysed as the dehydrated form **1**. Anal. Calc. for $C_{52}H_{43}Cl_2O_9P_2Ru$: C, 59.72; H, 4.14. Found: C, 59.57%; H, 4.38%. Selected IR bands/cm^{-1}: 3420(m, br), 1693(sh), 1669(s), 1653(s), 1609(s), 1404(m), 1269(m), 909(w), 807(m), 381(w), 352(s), 337(s). UV-Vis (DMF) λ_{max} (log ε): 300 nm (3.46). Suitable crystals of $\mathbf{1}\cdot 4H_2O$ for X-ray diffraction studies were obtained directly from the mother liquor.

Synthesis of $[RuCl_2(\mu\text{-}ox)_2La(H_2O)(dmf)_4]_n$ (2). A solution of $LaCl_3\cdot 9H_2O$ (18.57 mg, 0.05 mmol) in water (4 mL) is slowly poured over crystals of **1** (55.4 mg, 0.05 mmol) and then carefully layered with *N*,*N*-dimethylformamide (6 mL). Yellow crystals of **2** formed after 2 days and were collected by filtration, washed with acetone and dried in air. Yield: 50% Anal. Calc. for $C_{16}H_{34}N_4Cl_2O_{13}LaRu$: C, 23.98; H, 4.28; N, 6.99. Found: C, 23.62; H, 3.89; N, 6.85. Selected IR data/cm^{-1}: 1660(vs), 1635(s), 1609(s), 1422(m), 1383(m), 812(m). Crystals were very small but suitable for X-ray diffraction.

Synthesis of $[RuCl_2(\mu\text{-}ox)_2Dy(dmf)_4]_n$ (3). This complex was prepared by using the same procedure described for **2** but substituting $DyCl_3\cdot 6H_2O$ (18.1 mg, 0.05 mmol) for the lanthanum salt. Yellow

crystals of **3** were obtained with 75% yield. Anal. Calc. for $C_{32}H_{27}N_5Cl_4O_4DyRu$: C, 23.82; H, 4.00; N, 6.94. Found: C, 23.46; H, 3.66; N, 6.70. IR/cm^{-1}: peaks associated to the oxalato ligand appear at 1658(vs), 1605(vs), 1440(m), 1383(m) and 817(m). Crystals were very small but suitable for X-ray diffraction.

Crystallography.

The X-ray diffraction data for structures **1**-**3** were collected with a Rigaku SuperNOVA diffractometer with microfocus X-ray using CuKα radiation (λ = 1.54184 Å) for **1** and Mo Kα radiation (λ = 0.71073 Å) for **2** and **3**. CrysAlisPro[1] software was used to collect, index, scale and apply numerical absorption correction based on gaussian integration over a multifaceted crystal model and empirical absorption correction using spherical harmonics, implemented in SCALE3 ABSPACK scaling algorithm into CrysAlisPro. The structure was solved applying the novel dual-space algorithm implemented in SHELXT[2] program. Fourier recycling and least-squares refinement were used for the model completion with SHELXL[3]. All non-hydrogen atoms have been refined anisotropically, and all hydrogen atoms have been placed in geometrically suitable positions and refined riding with isotropic thermal parameter related to the equivalent isotropic thermal parameter of the parent atom. The geometrical analysis of interactions in the structure was performed with Olex2[4] program. The hydrogen atoms were geometrically positioned with C–H = 0.93 Å and Uiso(H) = 1.2 Ueq(C). Crystal data, collection procedures and refinement results are summarized in Table S1. Structures **2** and **3** contain dmf molecules, some of which show a certain degree of disorder that could be successfully modeled during the refinement.

Magnetic measurements.

Variable-temperature magnetic susceptibility measurements were carried out on polycrystalline samples using a Cryogenics SX600 SQUID magnetometer in the 1.8 to 300 K range. Experimental susceptibilities were corrected for the diamagnetism of the constituent atoms estimated from Pascal's constants and for the magnetization of the sample holder. Alternating current susceptibility measurements were performed under an oscillating ac field at frequencies ranging from 10 to 10000 Hz. A variable static field was applied parallel to the oscillating field.

Dynamic magnetic susceptibility data were analysed using the software package CC-Fit2 v3.1[5] with the generalized Debye model:[6,7]

$$\chi(\omega) = \chi_S + \frac{\chi_T - \chi_S}{(1 + i\omega\tau)^{1-\alpha}}$$

where χ_S and χ_T are the adiabatic and isothermal susceptibility, respectively, $\omega/2\pi$ is the frequency of the ac field, τ is the relaxation time and α is the width of the distribution times, which can take values between 0 and 1.

Computational calculations.

All quantum-chemical calculations were performed with the ORCA 6.0.1 program package[8]. Molecular models were extracted directly from the crystallographic structures, and no geometry optimization was applied to preserve the experimentally observed coordination environment.

To assess the magnetic anisotropy of compounds **1** and **2**, a CASSCF/SINGLE_ANISO[9] protocol was carried out on the isolated $[RuCl_2(ox)_2]^{3-}$ coordination fragments. All atoms were described with the def2-TZVP basis set[10] together with the Def2/JK[11] Coulomb fitting basis and the RIJK approximation. TightSCF criteria were employed to ensure stable convergence. The Ru^{III} active space consisted of five electrons in five orbitals, CAS(5,5), corresponding to the Ru^{III} 4d manifold. A state-averaged CASSCF calculation was performed, including 1 sextet, 15 quartet, and 10 doublet roots. Dynamic correlation was introduced through the strongly contracted NEVPT2 method[12]. Spin–orbit coupling (SOC) was treated using the quasi-degenerate perturbation theory approach within the SINGLE_ANISO module. Magnetic properties were computed from the resulting pseudospin Hamiltonian.

The magnetic exchange interaction between Dy^{III} and Ru^{III} in **3** was evaluated on the dinuclear fragment $[(ox)(dmf)_4Dy(\mu\text{-}ox)RuCl_2(ox)]^{2-}$ obtained from the crystal structure. In analogy with the methodology employed in related systems[13], DFT calculations were carried out using the Douglas–Kroll–Hess Hamiltonian of second order (DKH2) treatment[14] together with the following basis sets: SARC2-DKH-QZVP[15] for Dy, SARC-DKH-TZVP[16] for Ru, and DKH-Def2-TZVP[10] for the remaining atoms. The SARC/J auxiliary basis[17] was employed for Coulomb fitting, and the RIJCOSX approximation[18] was used to accelerate the hybrid functional calculations. A large integration grid (DEFGrid3) and TightSCF convergence criteria were applied throughout. Broken-symmetry DFT (BS-DFT) calculations were performed with a panel of six functionals to assess the robustness of the predictions: PBE0[19], B3LYP[20], CAM-B3LYP[21], TPSS0[22], M06[23] and ωB97M-V[24]. Atom-pairwise dispersion corrections (D4[25]; D3ZERO[26] for M06) were applied to all functionals except ωB97M-V, which includes dispersion inherently. High-spin (HS) and broken-symmetry (BS) solutions were converged using the flip-spin approach. Verification of the electronic states was carried out through Mulliken spin population analysis, which confirmed the expected inversion of the spin densities between the HS and BS states. The magnetic exchange coupling constant J was extracted using the Yamaguchi spin-projection formalism[27]

($\widehat{H} = -J(\hat{S}_1 \cdot \hat{S}_2)$), adopting the convention that positive J corresponds to ferromagnetic coupling.

To account for the strong anisotropy, the magnetic properties were subsequently simulated using the Lines model[28] [($\widehat{H} = -J_{LM}(\hat{\boldsymbol{s}}_1 \cdot \hat{\boldsymbol{s}}_2)$; $\hat{\boldsymbol{s}}_i$ are the *ab initio* spin operators for the low-lying exchange eigenstates] implemented in the POLY_ANISO ORCA module, starting from the isotropic exchange coupling constant derived from BS-DFT and local anisotropy parameters obtained via a diamagnetic substitution strategy. To isolate the single-ion magnetic properties, two independent computational models were analyzed: one characterizing the Dy(III) center by substituting Ru^{III} with diamagnetic Ga^{III}, and a second characterizing the Ru^{III} center by substituting Dy^{III} with diamagnetic La^{III}. In both cases, CASSCF/NEVPT2/SINGLE_ANISO calculations were performed utilizing the def2-TZVP basis set combined with the RIJK approximation and the Def2/JK auxiliary basis. For the Dy^{III} model, the active space comprised nine electrons in seven 4*f* orbitals, with state averaging performed over 21 sextet (S = 5/2), 10 quartet (S = 3/2), and 5 doublet (S = 1/2) roots. For the Ru^{III} model, the active space definition was identical to that described above for the mononuclear $[RuCl_2(ox)_2]^{3-}$ fragment.

Table S1. Crystallographic data and structure refinement for **1**·4H_2O, **2** and **3**.

Compound	**1**·4H_2O	**2**	**3**
Empirical formula	$C_{52}H_{51}Cl_2O_{13}P_2Ru$	$C_{16}H_{30}N_4O_{13}Cl_2RuLa$	$C_{16}H_{28}N_4O_{12}Cl_2RuDy$
Formula weight	1117.83	797.31	802.89
T/K	298.0(5)	298.0(5)	298.0(5)
λ/Å	1.54184	0.71073	0.71073
Crystal system	Triclinic	Triclinic	Othorhombic
Space group	*P-1*	*P-1*	$Pna2_1$
a /Å	9.7876(3)	11.1623(7)	10.6127(2)
b /Å	14.6019(5)	12.4160(7)	14.5103(3)
c /Å	19.0198(5)	12.6227(8)	18.1012(3)
α /°	84.823(2)	89.742(5)	90
β /°	75.818(2)	65.308(6)	90
γ /°	84.852(3)	67.666(6)	90
Volume /Å^3	2618.22(14)	1445.24(19)	2787.47(9)
Z	2	2	4
ρ_{calcd}/g cm^{-3}	1.418	1.832	1.913
μ/mm^{-1}	4.461	2.222	3.453
F(000)	1150	784	1568
Crystal size /mm^3	0.21 x 0.11 x 0.08	0.16 x 0.08 x 0.06	0.15 x 0.05 x 0.03
2θ range for data collection/°	7.49 to 143.74	3.6 to 57.4	3.6 to 57.4
Index ranges	-9 ≤ *h* ≤ 12 -18 ≤ *k* ≤ 17 -22 ≤ *l* ≤ 23	-14 ≤ *h* ≤ 15 -15 ≤ *k* ≤ 16 -11 ≤ *l* ≤ 17	-14 ≤ *h* ≤ 12 -19 ≤ *k* ≤ 19 -24 ≤ *l* ≤ 22
Reflect. collected	20036	13575	15933
Independent reflect. [*R*(int)]	9963 [0.0239]	7457 [0.0208]	6490 [0.0302]
Data/restraints/ parameters	9963/3/668	7457/40/367	6490/105/379
[a]Goodness-of-fit on F^2	1.030	1.034	1.040
[b]Final *R* indices [$I > 2\sigma(I)$]	R_1 = 0.0329, wR_2 = 0.0856	R_1 = 0.0317, wR_2 = 0.0670	R_1 = 0.0325, wR_2 = 0.0594
R indices (all data)	R_1 = 0.0392, wR_2 = 0.0921	R_1 = 0.0385, wR_2 = 0.0705	R_1 = 0.0418, wR_2 = 0.0634
Flack Parameter	-	-	-0.013(8)
Largest diff. peak and hole/e Å^{-3}	0.58 /-0.54	1.02 / -0.64	0.56 / -0.56

[a]Goodness-of-fit: $S = \sqrt{\frac{\sum[w(F_o^2 - F_c^2)^2]}{(N-P)}}$; [b] $R = \frac{\sum||F_o|-|F_c||}{\sum|F_o|}$ and $R_w = \sqrt{\frac{\sum[w(F_o^2 - F_c^2)^2]}{\sum[w(F_o^2)^2]}}$.

Table S2. Selected interatomic distances (Å) and angles (°) for **1**·4H_2O.

Distances (Å)			
Ru1-Cl1	2.3410(7)	Ru2-Cl2	2.3396(7)
Ru1-Cl1^{i}	2.3410(7)	Ru2-Cl2^{ii}	2.3396(7)
Ru1-O1	2.0513(15)	Ru2-O5	2.0486(15)
Ru1-O1^{i}	2.0512(15)	Ru2-O5^{ii}	2.0486(15)
Ru1-O2	2.0433(15)	Ru2-O6	2.0469(15)
Ru1-O2^{i}	2.0432(15)	Ru2-O6^{ii}	2.0468(15)
Angles (°)			
Cl1-Ru1-Cl1i	180	Cl2-Ru2-Cl2^{ii}	180
O1-Ru1-Cl1	90.95(6)	O5-Ru2-Cl2	90.41(6)
O2-Ru1-Cl1	90.76(5)	O6-Ru2-Cl2	89.55(6)
O2-Ru1-O1	80.36(6)	O6-Ru2-O5	80.23(6)

(i): 1 – x, 1 – y, 1 – z; (ii): 2 – x, 2 – y, – z.

Table S3. Selected interatomic distances (Å) and angles (°) for **2**.

Distances (Å)			
Ru1-Cl1	2.3550(10)	Ru2-Cl2	2.3450(10)
Ru1-Cl1^{i}	2.3550(10)	Ru2-Cl2^{ii}	2.3450(10)
Ru1-O3	2.056(2)	Ru2-O7	2.051(2)
Ru1-O3^{i}	2.056(2)	Ru2-O7^{ii}	2.051(2)
Ru1-O4	2.049(2)	Ru2-O8	2.059(2)
Ru1-O4^{i}	2.049(2)	Ru2-O8^{ii}	2.059(2)
La1-O1	2.604(2)	La1-O10	2.532(2)
La1-O2	2.590(2)	La1-O11	2.467(3)
La1-O5	2.557(2)	La1-O12	2.519(2)
La1-O6	2.658(2)	La1-O1W	2.525(2)
La1-O9	2.489(3)		
Angles (°)			
Cl1^{i}-Ru1-Cl1	180	Cl2^{ii}-Ru2-Cl2	180
O3-Ru1-Cl1	90.95(8)	O7-Ru2-Cl2	90.55(8)
O4-Ru1-Cl1	92.41(7)	O8-Ru-Cl2	88.37(8)
O4-Ru1-O3	80.84(8)	O7-Ru2-O8	80.38(8)
O1-La1-O1W	130.08(7)	O10-La1-O11	72.50(9)
O1-La1-O6	106.47(7)	O10-La1-O12	71.56(10)
O2-La1-O6	66.76(7)	O10-La1-O1W	71.25
O5-La1-O1W	132.10(7)	O11-La1-O12	87.51(10)
O9-La1-O11	84.48(11)	O11-La1-O1W	143.14(8)
O9-La1-O12	139.28(9)		

(i): – x, – y, 1 – z; (ii): – x, 1 – y, –z.

Table S4. Selected interatomic distances (Å) and angles (°) for **3**.

Distances (Å)			
Ru1-Cl1	2.3375(18)	Ru1-Cl2	2.339(2)
Ru1-O1	2.067(5)	Ru1-O3	2.056(4)
Ru1-O5	2.063(4)	Ru1-O7	2.052(4)
Dy1-O2	2.420(4)	Dy1-O11	2.354(3)
Dy1-O4	2.418(4)	Dy1-O21	2.342(4)
Dy1-O6^{i}	2.409(4)	Dy1-O31	2.277(3)
Dy1-O8^{i}	2.413(4)	Dy1-O41A	2.329(8)
		Dy1-O41B	2.331((12)
Angles (°)			
Cl1-Ru1-Cl2	179.48(7)	O3-Ru1-O5	179.0(2)
O1-Ru1-Cl1	89.84(15)	O3-Ru1-O7	99.88(17)
O1-Ru1-Cl2	89.71(15)	O5-Ru1-Cl1	92.10(12)
O3-Ru1-Cl1	87.17(14)	O5-Ru1-Cl2	88.23(13)
O3-Ru1-Cl2	89.71(15)	O7-Ru1-Cl1	89.75(15)
		O7-Ru1-Cl2	90.70(14)
O2-Dy1-O6^{i}	107.49(15)	O11-Dy1-O6^{i}	139.87(15)
O2-Dy1-O8^{i}	75.37(12)	O11-Dy1-O8^{i}	75.48(15)
O4-Dy1-O6^{i}	70.54(11)	O21-Dy1-O6^{i}	80.37(15)
O4-Dy1-O8^{i}	109.40(16)	O21-Dy1-O8^{i}	76.42(16)
O8^{i}-Dy1-O6^{i}	67.02(15)	O31-Dy1-O6^{i}	76.44(15)
		O31-Dy1-O8^{i}	136.19(15)

(i): 1 – x, 1 – y, 1/2 + z.

Table S5. Analysis of the coordination environment (coordination number = 9) of lanthanum ion in **2** by means of the CShM parameters obtained from the SHAPE software[29].

TCTPR-9	MFF-9	CSAPR-9	JCSAPR-9	JTCTPR-9	JCCU-9	CCU-9	HH-9	JTDIC-9	OPY-9	JTC-9	HBPY-9	EP-9
7.107	7.349	7.432	9.078	10.640	14.892	14.930	15.952	16.764	18.547	20.126	22.173	28.858

TCTPR = Spherical tricapped trigonal prism, MFF = Muffin, CSAPR = Spherical capped square antiprism, JCSAPR = Capped square antiprism J10, JTCTPR = Tricapped trigonal prism J51, JCCU = Capped cube J8, CCU = Spherical-relaxed capped cube, HH = Hula-hoop, JTDIC = Tridiminished icosahedron J63, OPY = Octagonal Pyramid, JTC = Triangular cupola J3, HBPY = Heptagonal bipyramid and EP = Enneagon.

Table S6. Analysis of the coordination environment (coordination number = 8) of the dysprosium ion in **3** by means of the CShM parameters obtained from the SHAPE software[30].

SAPR-8	BTPR-8	TDD-8	JBTPR-8	JSD-8	CU-8	TT-8	JGBF-8	HBPY-8	HPY-8	ETBPY-8	JETBPY-8	OP-8
0.341	2.001	2.075	2.770	4.892	10.137	10.972	15.754	16.524	22.897	23.036	27.749	28.724

SAPR-8 = Square antiprism, BTPR-8 = Biaugmented trigonal prism, TDD-8 = Triangular dodecahedron, JBTPR-8 = Biaugmented trigonal prism J50, JSD-8 = Snub diphenoid J84, CU-8 = Cube, TT-8 = Triakis tetrahedron, JGBF-8 = Johnson-Gyrobifastigium J26, HBPY-8 = Hexagonal bipyramid, HPY-8 = Heptagonal pyramid, ETBPY-8 = Elongated trigonal bipyramid, JETBPY-8 = Johnson elongated triangular bipyramid J14 and OP-8 = Octagon.

Table S7. CAS-SCF calculated energies and of the d-orbital field splitting for $[RuCl_2(ox)_2]^{3-}$ units in **1** and **2**.

			Loewdin orbital-compositions				
	Orbital #	Energy (Eh)	d_{z^2}	$d_{x^2-y^2}$	d_{xz}	d_{yz}	d_{xy}
Ru(1) in **1**	68	0.11667	2.0	92.0	0.0	0.0	0.0
	69	0.14087	0.0	0.1	8.4	84.0	0.0
	70	0.14634	0.1	0.0	83.4	8.5	0.0
	71	0.33414	74.3	1.5	0.1	0.0	0.2
	72	0.39484	0.2	0.0	0.0	0.0	79.5
Ru(2) in **1**	68	0.11893	1.9	92.1	0.0	0.0	0.0
	69	0.14407	0.0	0.0	0.1	92.3	0.0
	70	0.14834	0.1	0.0	91.6	0.0	0.0
	71	0.33894	74.2	1.4	0.1	0.0	0.0
	72	0.39701	0.0	0.0	0.0	0.0	79.6
Ru(1) in **2**	68	0.11097	1.5	90.8	1.5	0.5	0.0
	69	0.13549	0.3	1.4	25.6	65.2	0.0
	70	0.14115	0.1	0.4	64.8	26.9	0.0
	71	0.32995	74.0	1.3	0.1	0.0	0.7
	72	0.38486	0.6	0.0	0.0	0.0	79.2
Ru(2) in **2**	68	0.11089	1.9	92.0	0.2	0.2	0.0
	69	0.13603	0.0	0.4	20.6	71.3	0.0
	70	0.13997	0.1	0.0	71.1	20.9	0.0
	71	0.33300	73.8	1.4	0.0	0.1	0.6
	72	0.38088	0.5	0.0	0.0	0.0	79.5

Table S8. QDPT/NEVPT2 calculated energies of the lowest energy levels for both crystallographic $[RuCl_2(ox)_2]^{3-}$ units in **1** and main values of g-tensors in the three low-lying Kramer doublets (KD), calculated within the pseudo-spin S = ½ formalism. θ is the angle between the principal magnetic *Z* axis of each KD and the principal magnetic *Z* axis of the first one.

Level	Relative Energy (cm^{-1})	g_X	g_Y	g_Z	θ (°)
1.1	0.00	2.08379772	2.07425359	1.99584280	0
2.1	1822.48	1.84906638	1.95266256	2.42988779	0.9980
3.1	1996.95	1.93432364	1.88224764	1.56249036	1.1149
4.1	12077.57				
5.1	15111.33				
6.1	15775.12				
1.2	0.00	2.08072138	2.07515900	1.99587330	0
2.2	1845.70	1.84947582	1.95092181	2.43978023	1.0461
3.2	2016.73	1.93251246	1.87818700	1.55281775	1.2316
4.2	12461.75				
5.2	15523.32				
6.2	16105.39				

Table S9. QDPT/NEVPT2 calculated energies of the lowest energy levels for both crystallographic $[RuCl_2(ox)_2]^{3-}$ units in **2** and main values of g-tensors in the three low-lying Kramer doublets (KD), calculated within the pseudo-spin S = ½ formalism. θ is the angle between the principal magnetic *Z* axis of each KD and the principal magnetic *Z* axis of the first one.

Level	Relative Energy (cm^{-1})	g_X	g_Y	g_Z	θ (°)
1.1	0.00	2.10278985	2.06056150	1.99551504	0
2.1	1525.40	1.89026699	2.00068134	2.08909769	179.8738
3.1	2359.96	1.99794543	1.93706708	1.90359505	1.0914
4.1	11988.48				
5.1	15018.98				
6.1	15647.40				
1.2	0.00	2.07959599	2.07104695	1.99600753	0
2.2	1931.61	1.85746921	1.95740704	2.42147478	0.4475
3.2	2110.08	1.94120206	1.88293624	1.57198349	0.5182
4.2	12379.75				
5.2	15158.42				
6.2	15756.59				

Table S10. Predicted magnetic properties for the dinuclear fragment $[(ox)(dmf)_4Dy(\mu\text{-}ox)RuCl_2(ox)]^{2-}$.

Functional	DFT-BS $J_{Ru\text{-}Dy}$ (cm^{-1})	Exchange Interaction (Lines model) $J^{LM}_{Ru\text{-}Dy}$ (cm^{-1})			Dipole-Dipole interaction			Total Magnetic interaction (cm^{-1})	
		Isotropic (5%)	Symmetric (50%)	Anti-Symmetric (45%)	Isotropic (9%)	Symmetric (56%)	Anti-Symmetric (36%)	E_1-E_4 *gap*	*Lowest doublet splitting*
B3LYP-D4	+0.48	−0.15	−0.61 to +0.45	Max. 0.54	−0.02	−0.04 to +0.04	Max. 0.03	0.65	0.004
PBE0-D4	+0.04	−0.01	−0.05 to +0.04	Max. 0.05				0.09	0.0002
TPSS0-D4	+0.04	−0.01	−0.05 to +0.04	Max. 0.05				0.09	0.0002
M06-D3ZERO	+0.30	−0.10	−0.38 to +0.28	Max. 0.34				0.42	0.003
wB97M-V	+0.34	−0.11	−0.43 to +0.32	Max. 0.38				0.47	0.003
CAM-B3LYP-D4	+0.10	−0.03	−0.13 to +0.09	Max. 0.11				0.17	0.0008

All employed functionals predict a positive value for the isotropic exchange constant $J_{Ru\text{-}Dy}$, ranging from +0.04 cm^{-1} (PBE0, TPSS0) to +0.48 cm^{-1} (B3LYP). In a purely spin-only formalism, this would suggest a ferromagnetic exchange. However, this scalar *J* value does not fully describe the interaction with a highly anisotropic Dy^{III} ion.

Contrary to the BS-DFT spin-only prediction, the Lines model reveals a more complex picture. The isotropic component of the effective interaction between the ground doublets is consistently negative across all functionals (from –0.01 to –0.15 cm^{-1}) indicating an effective antiferromagnetic coupling. Furthermore, the interaction is highly anisotropic. The decomposition shows that the symmetric (anisotropic exchange) and antisymmetric (Dzyaloshinskii-Moriya-like) terms dominate the interaction, displaying significant relative weights of approximately 50% and 45%, respectively.

Additionally, the through-space dipole-dipole interaction plays a non-negligible role in these weakly coupled systems. With an isotropic term of approximately –0.02 cm^{-1}, the dipolar contribution is comparable in magnitude to the exchange interaction, further reinforcing the antiferromagnetic nature of the coupling.

Lastly, the calculated total energy splitting between the ground and first excited coupled states (E_1-E_4 gap) lies between 0.09 cm^{-1} (PBE0/TPSS0) and 0.65 cm^{-1} (B3LYP). This small gap confirms that the antiferromagnetic exchange interaction is subtle and easily masked by the large intrinsic anisotropy of the dysprosium center.

Table S11. Parameters obtained from fitting ac susceptibility data of **1** to the generalised Debye model varying the temperature at constant dc-field (1 kOe).‡

T (K)	τ (ms)	τ_+ (ms)	τ_- (ms)	χ_S ×10^3	σ_{χ_S} x10^3	χ_T	σ_{χ_T}	α	σ_α
2.00	7.465	20.648	2.699	1.00	0.80	0.266	0.005	0.200	0.010
2.30	5.165	14.355	1.858	1.59	0.81	0.235	0.003	0.201	0.010
2.61	4.653	15.907	1.361	0.38	1.27	0.232	0.005	0.254	0.016
2.92	3.100	8.402	1.144	2.05	1.34	0.197	0.004	0.195	0.017
3.23	2.174	5.480	0.862	1.55	0.84	0.171	0.002	0.175	0.011
3.50	1.765	3.644	0.855	1.63	1.30	0.153	0.002	0.122	0.018
3.80	1.189	2.592	0.545	2.24	0.94	0.146	0.001	0.137	0.013
4.11	0.858	2.029	0.363	0.78	1.84	0.136	0.002	0.158	0.024
4.43	0.563	0.993	0.319	2.39	1.09	0.118	0.001	0.082	0.015
4.74	0.431	0.828	0.224	1.32	0.66	0.115	0.001	0.104	0.009
5.06	0.305	0.563	0.165	1.08	1.40	0.106	0.001	0.093	0.019
5.37	0.219	0.370	0.129	0.93	1.71	0.099	0.001	0.072	0.023
5.69	0.157	0.234	0.105	1.61	2.84	0.091	0.002	0.044	0.040
6.00	0.120	0.185	0.078	1.16	0.94	0.088	0.001	0.050	0.013
6.50	0.084	0.126	0.056	0.37	2.27	0.080	0.001	0.045	0.030
7.00	0.057	0.077	0.042	1.35	1.32	0.073	0.000	0.027	0.017
7.50	0.039	0.057	0.027	0.00	2.11	0.069	0.001	0.039	0.024
8.00	0.029	0.052	0.016	0.00	6.90	0.067	0.001	0.084	0.067
8.50	0.021	0.021	0.021	0.91	3.06	0.059	0.000	0.000	0.030

‡ In Tables S11-S15, τ_+ y τ_- are the upper and lower values for the relaxation time, respectively, as estimated by CCFit2; χ_S, χ_T are given in cm^{3}mol^{-1} and σ_{χ_S}, σ_{χ_T} and σ_α are the uncertainties in χ_S, χ_T, and α, respectively.

Table S12. Parameters obtained from fitting ac susceptibility data of **1** to the generalised Debye model varying the temperature at constant dc-field (2 kOe).

T (K)	τ (ms)	τ_+ (ms)	τ_- (ms)	χ_S ×10^3	σ_{χ_S} x10^3	χ_T	σ_{χ_T}	α	σ_α
2.00	12.824	35.481	4.635	0.000	1.145	0.293	0.011	0.200	0.018
2.30	7.290	18.443	2.882	0.711	0.969	0.232	0.005	0.176	0.014
2.61	6.005	15.604	2.311	0.000	0.984	0.219	0.005	0.184	0.014
2.92	4.023	9.766	1.657	0.600	0.533	0.191	0.002	0.165	0.008
3.23	2.810	6.495	1.215	0.791	1.051	0.168	0.003	0.152	0.015
3.50	2.386	4.595	1.238	0.619	0.798	0.152	0.002	0.104	0.012
3.80	1.369	2.654	0.706	1.181	1.528	0.141	0.002	0.106	0.022
4.11	1.043	2.239	0.486	0.138	1.932	0.137	0.003	0.133	0.026
4.43	0.693	1.232	0.390	0.879	1.393	0.121	0.002	0.084	0.020
4.74	0.462	0.718	0.297	1.203	0.726	0.111	0.001	0.053	0.011
5.06	0.332	0.489	0.225	1.678	0.668	0.106	0.001	0.042	0.010
5.37	0.232	0.366	0.147	0.292	0.969	0.098	0.001	0.056	0.014
5.69	0.175	0.295	0.104	0.000	1.494	0.096	0.001	0.070	0.021
6.00	0.129	0.190	0.087	0.503	0.739	0.088	0.000	0.042	0.010
6.50	0.095	0.162	0.056	0.000	4.115	0.083	0.002	0.073	0.054
7.00	0.058	0.074	0.046	0.983	1.242	0.073	0.001	0.016	0.016
7.50	0.040	0.046	0.035	1.436	1.663	0.067	0.000	0.006	0.020
8.00	0.029	0.041	0.020	0.000	1.693	0.065	0.000	0.033	0.018
8.50	0.021	0.021	0.021	0.597	3.473	0.059	0.001	0.000	0.034

Table S13. Parameters obtained from fitting ac susceptibility data of **1** to the generalised Debye model varying the dc-field at 2.0 K.

H (Oe)	τ (ms)	τ_+ (ms)	τ_- (ms)	χ_S ×10^3	σ_{χ_S} x10^3	χ_T	σ_{χ_T}	α	σ_α
200	5.948	19.647	1.801	23.64	0.91	0.267	0.004	0.165	0.012
300	7.173	26.477	1.943	10.90	0.65	0.277	0.004	0.188	0.008
400	8.986	36.121	2.235	6.00	0.52	0.294	0.004	0.207	0.007
500	8.470	31.279	2.293	4.04	0.66	0.268	0.004	0.189	0.009
600	9.332	35.467	2.456	2.42	0.53	0.272	0.004	0.195	0.008
700	9.640	33.532	2.771	2.30	0.51	0.264	0.004	0.176	0.008
800	13.655	58.327	3.197	0.79	0.47	0.304	0.005	0.219	0.007
900	13.298	53.140	3.328	1.03	0.38	0.291	0.004	0.205	0.006
1000	14.873	61.821	3.578	0.51	0.57	0.297	0.007	0.214	0.009
1100	15.070	58.932	3.854	0.93	0.54	0.291	0.006	0.201	0.009
1200	15.034	53.855	4.197	1.30	0.65	0.281	0.008	0.182	0.012
1300	17.856	75.247	4.237	0.00	0.28	0.288	0.004	0.216	0.005
1400	28.746	150.429	5.493	0.00	0.80	0.366	0.020	0.261	0.015
1500	22.691	102.297	5.033	0.00	0.66	0.320	0.012	0.231	0.012
1600	24.972	115.469	5.401	0.00	0.48	0.322	0.010	0.236	0.009
1700	19.612	74.227	5.182	0.98	0.52	0.283	0.008	0.194	0.011
1800	20.921	86.376	5.067	0.10	0.35	0.284	0.006	0.212	0.007

Table S14. Parameters obtained from fitting ac susceptibility data of **2** to the generalised Debye model varying the temperature at constant dc-field (2 kOe).

T (K)	τ (ms)	τ_+ (ms)	τ_- (ms)	χ_S ×10^3	σ_{χ_S} x10^3	χ_T	σ_{χ_T}	α	σ_α
2.00	3.401	37.088	0.312	34.2	3.8	0.251	0.013	0.395	0.039
2.24	2.528	26.562	0.241	29.6	2.8	0.232	0.008	0.389	0.028
2.52	1.620	9.889	0.266	30.4	2.3	0.194	0.004	0.292	0.027
2.82	1.089	5.670	0.209	26.7	1.7	0.172	0.003	0.260	0.021
3.17	0.591	2.106	0.166	24.5	2.0	0.146	0.002	0.181	0.027
3.55	0.377	1.532	0.093	18.8	1.3	0.136	0.001	0.209	0.016
3.99	0.223	0.719	0.069	17.4	0.8	0.120	0.001	0.159	0.010
4.47	0.138	0.452	0.042	13.5	1.5	0.108	0.001	0.163	0.018
5.02	0.089	0.219	0.036	13.0	1.9	0.093	0.001	0.105	0.025
5.63	0.060	0.139	0.026	11.0	0.8	0.083	0.000	0.092	0.011
6.31	0.042	0.093	0.019	9.4	2.4	0.074	0.001	0.082	0.031
7.08	0.030	0.077	0.012	6.0	3.8	0.067	0.001	0.112	0.042
7.95	0.019	0.065	0.006	0.1	19.0	0.061	0.003	0.172	0.161

Table S15. Parameters obtained from fitting ac susceptibility data of **2** to the generalised Debye model varying the dc-field at 2.0 K.

H (Oe)	τ (ms)	τ_+ (ms)	τ_- (ms)	χ_S ×10^3	σ_{χ_S} x10^3	χ_T	σ_{χ_T}	α	σ_α
500	5.091	123.112	0.211	159.4	2.5	0.258	0.011	0.505	0.053
750	2.656	25.630	0.275	119.9	2.9	0.240	0.008	0.375	0.052
1000	4.279	66.420	0.276	86.6	1.8	0.256	0.007	0.448	0.024
1250	5.891	77.440	0.448	69.3	1.7	0.284	0.008	0.424	0.021
1500	4.056	40.702	0.404	55.0	2.4	0.258	0.009	0.382	0.028
1750	4.622	49.882	0.428	41.9	1.5	0.261	0.006	0.394	0.018
2000	4.412	44.433	0.438	34.9	1.5	0.255	0.006	0.382	0.018
2250	4.665	51.094	0.426	25.9	2.0	0.261	0.008	0.396	0.021
2500	5.182	54.747	0.490	23.5	1.1	0.264	0.005	0.390	0.012
2750	4.144	34.018	0.505	20.6	2.5	0.247	0.009	0.347	0.028
3000	3.689	30.388	0.448	17.4	1.7	0.226	0.006	0.348	0.020

Figure S1. FT-IR spectrum of **1** recorded as KBr pellets (top) and UV-Vis absorption spectrum of a 0.1 mM solution of **1** in dmf (below).

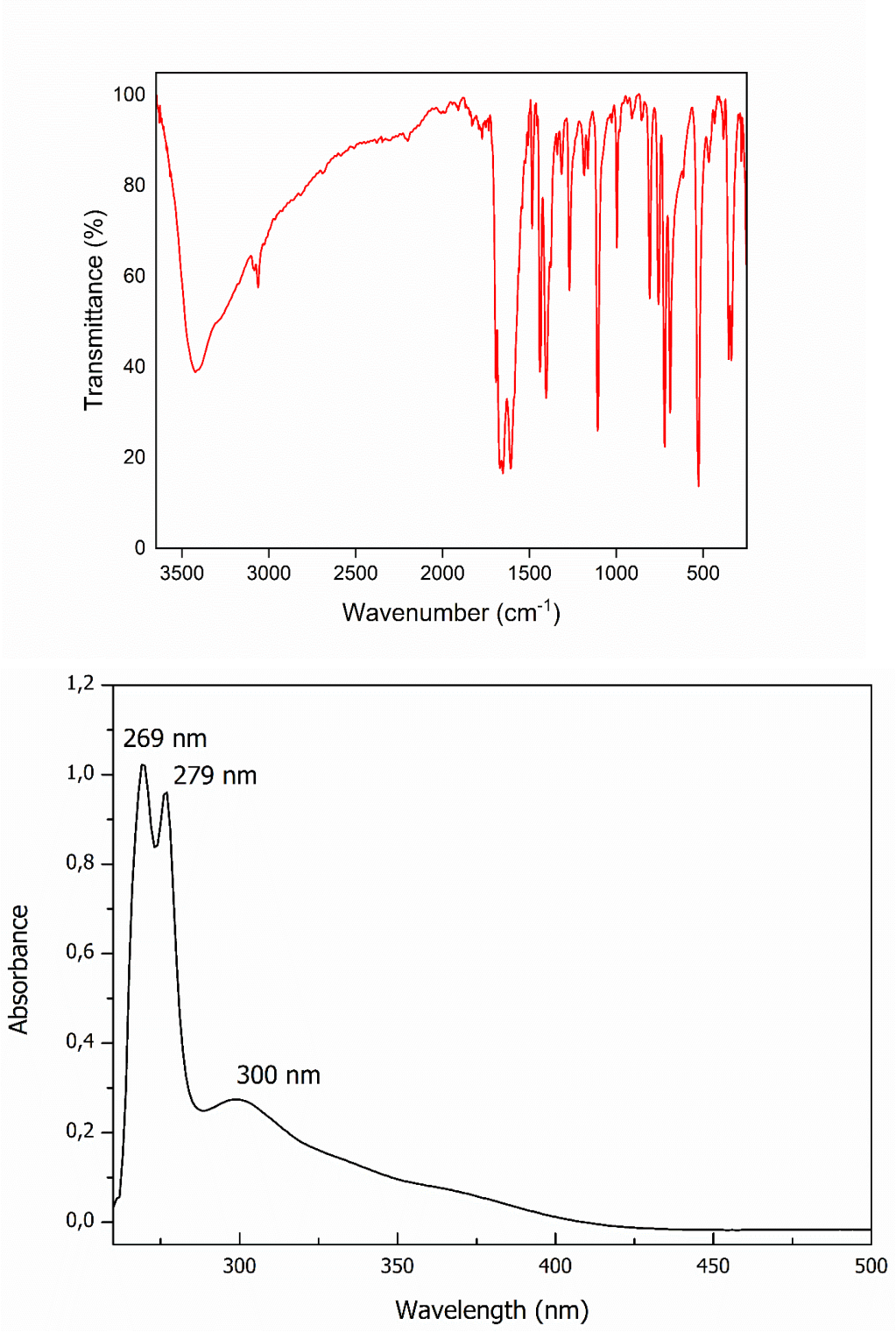

Figure S2. FT-IR spectra of **2** (top) and **3** (bottom) recorded as KBr pellets.

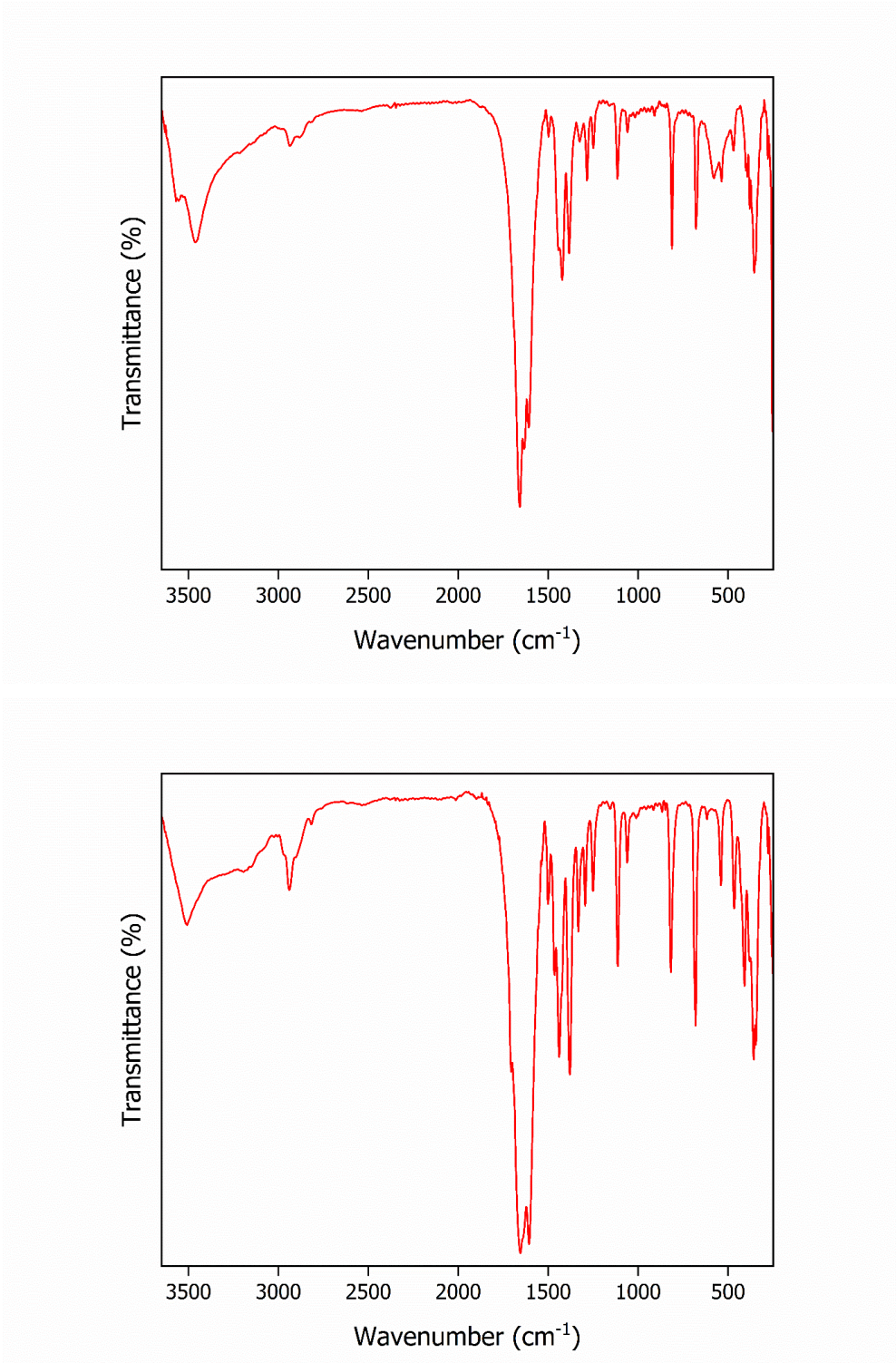

Figure S3. Perpective drawing of cristallographically non-equivalent *trans*-$[RuCl_2(ox)_2]^{3-}$ units in **1**·$4H_2O$ (top), **2** (middle), and **3** (bottom), showing the atom numbering. Thermal ellipsoids are plotted at 50 % probability level. For complexes **1** and **2**, each ruthenium atom lies on an inversion center.

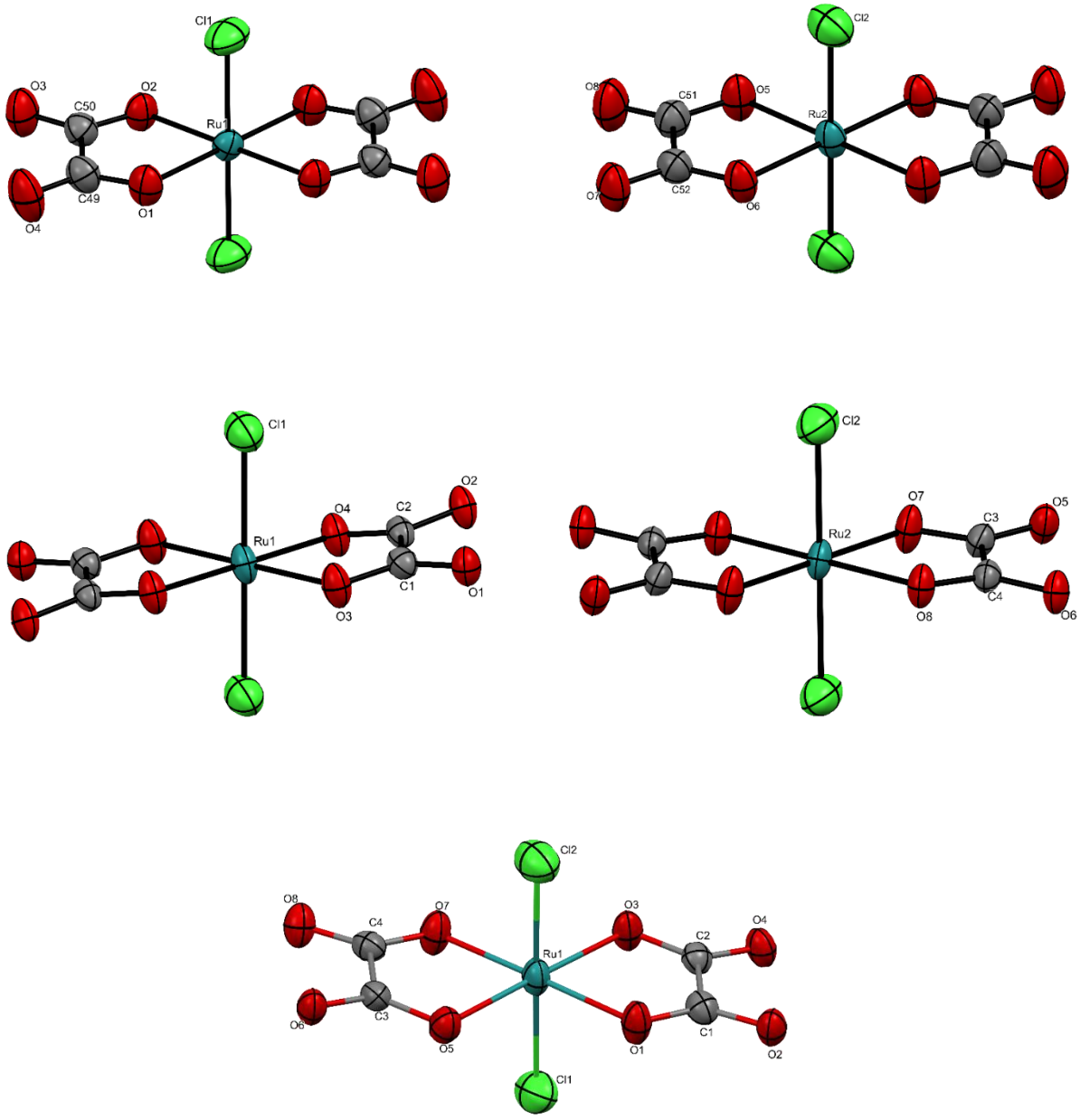

Figure S4. (a) Perspective view of the unit cell of **1**·4H_2O. The two crystallographically non-equivalent ruthenium atoms are Ru1, located at the cell center, and Ru2, located at the cell corners. This compound is formulated as $(PPh_4)_2(H_3O)[RuCl_2(ox)_2]\cdot 4H_2O$ for simplicity, since the solid loses four water molecules upon stored in a desiccator. However, $[RuCl_2(ox)_2]^{3-}$ crystallizes as a double salt containing tetraphenylphosphonium and zundel cations ($H_5O_2^+$). Color code: Ru cyan, Cl green, O(oxalate) red, O(water) sky blue, C gray, P yellow. Hydrogens atoms were omitted for clarity. (b) View of one layer of $[RuCl_2(ox)_2]^{3-}$ anions, $H_5O_2^+$ cations, and water molecules parallel to the (0 1 1) plane in **1**·4H_2O. Hydrogen atoms are shown in light gray and hydrogen bonds are depicted as blue dashed lines.

(a)

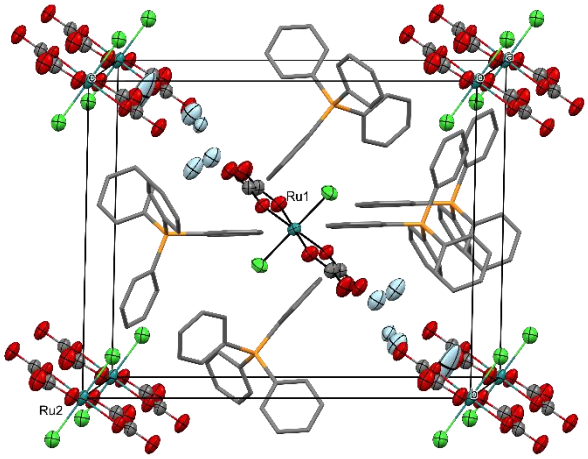

(b)

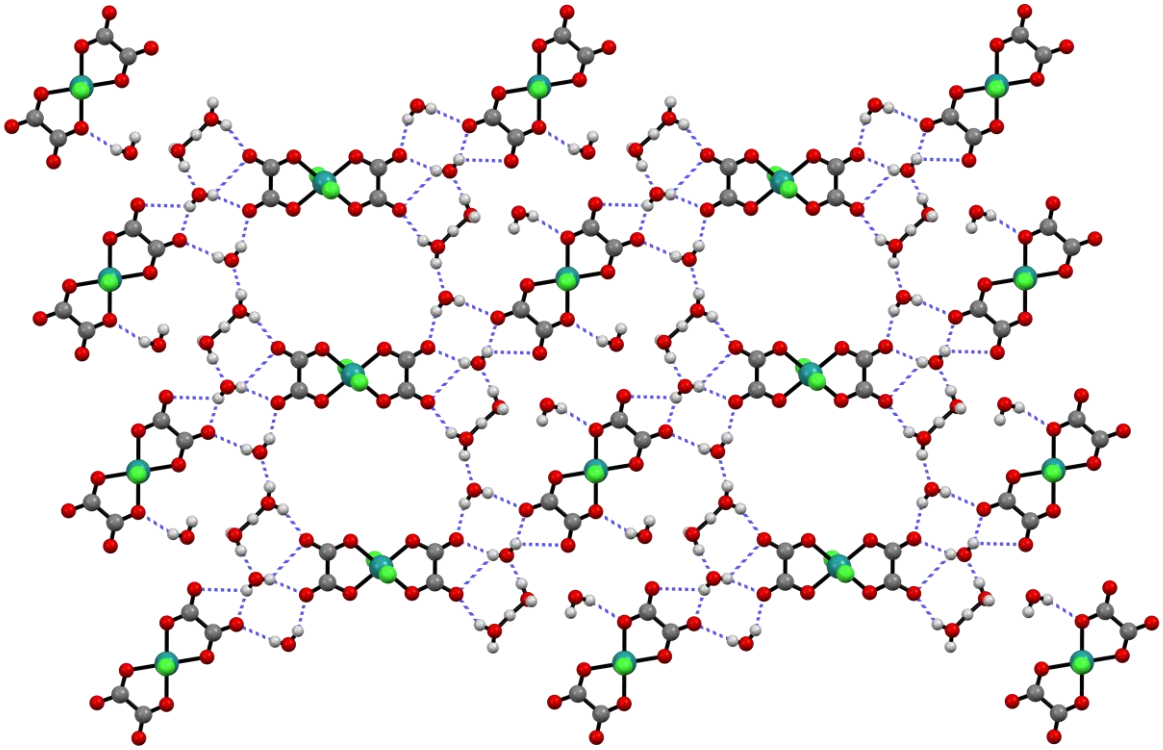

Figure S5. (a) Perspective drawing of a fragment of **2**, showing the atom numbering. Thermal ellipsoids are plotted at 50 % probability level. (b) Coordination polyhedron around the La^{III} center in **2**. (c, d, e) View of the packing of chains in **2** along the a, b, and c axes, respectively; each chain is shown in a different color, and the dmf molecules are depicted as capped sticks.

(a)

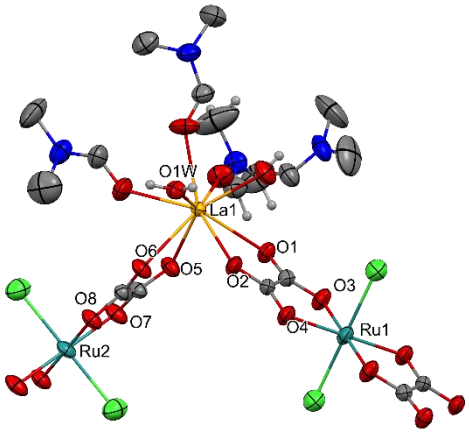

(b)

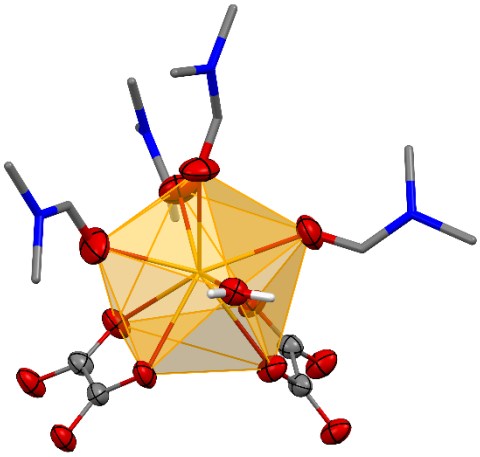

(c)

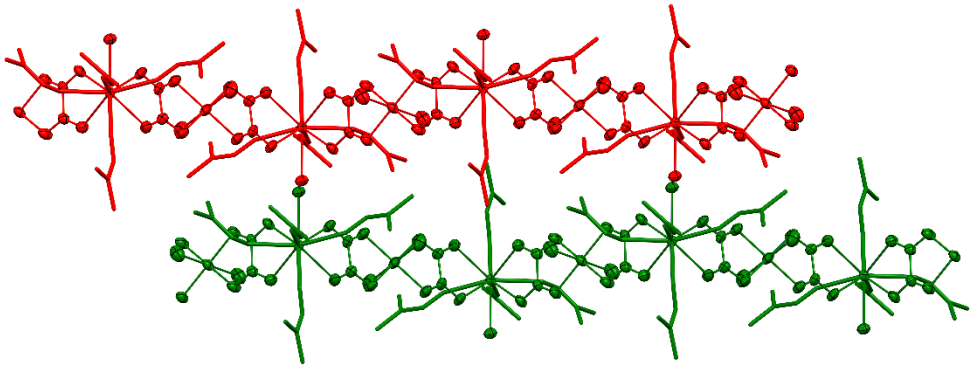

(d)

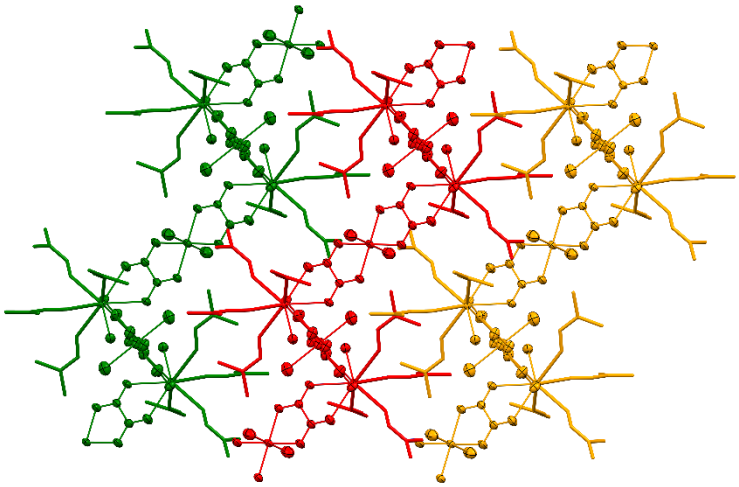

(e)

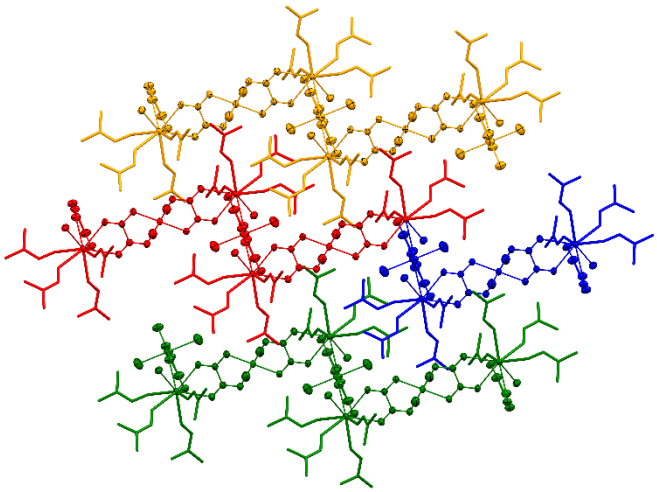

Figure S6. (a) View of a fragment of the heterobimetallic chain of **3**. Color code: Ru cyan, Cl green, O red, C gray, Dy pink, N blue. H atoms were ommited for clarity. (b) Perpective drawing of a fragment of **3** showing the atom numbering. Thermal ellipsoids are plotted at 50 % probability level. (c) Coordination polyhedron around the Dy^{III} center in **3**. (d, e, f) View of the packing of chains in **3** along the a, b, and c axes, respectively; each chain is shown in a different color, and the dmf molecules are depicted as capped sticks.

(a)

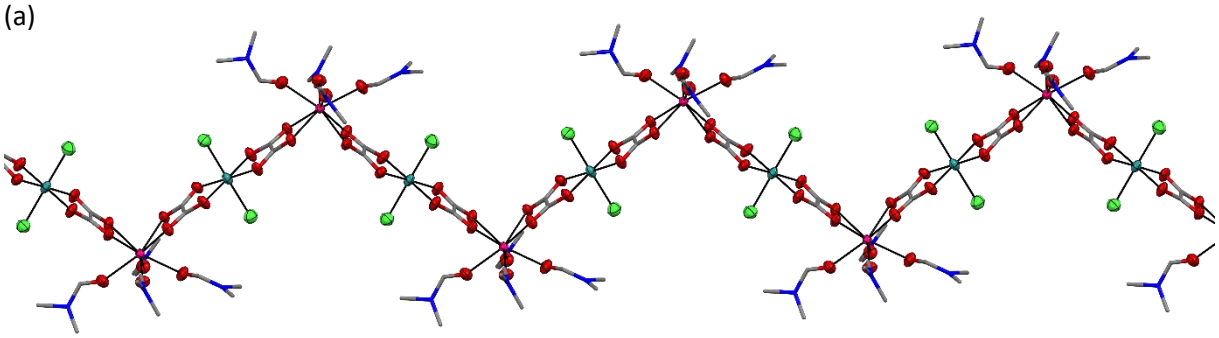

(b)

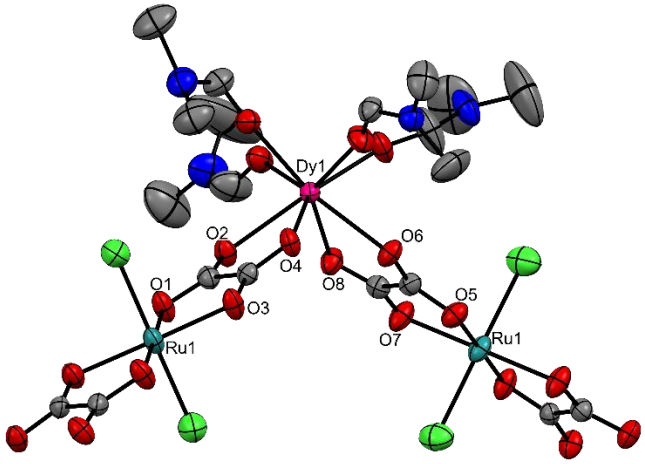

(c)

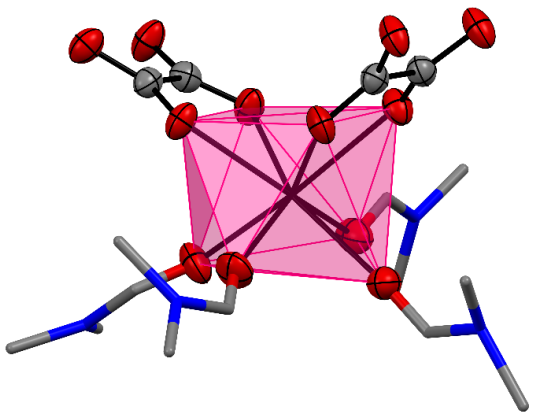

(d)

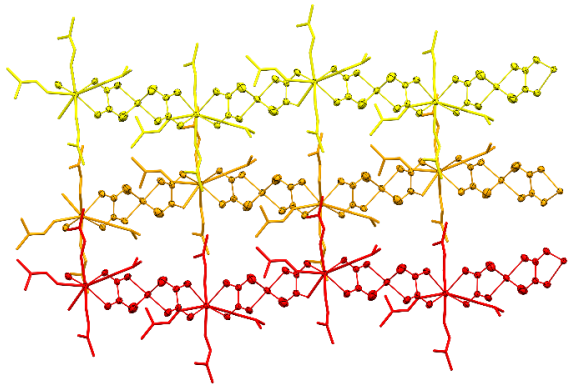

(e)

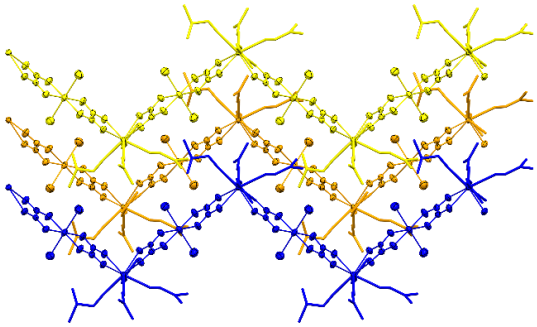

(f)

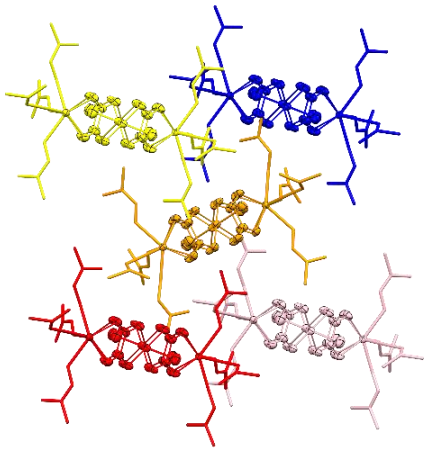

Figure S7. (a) Thermal dependence of $\chi_M T$ for **1** measured under an applied field of 1.0 kOe. Inset: Magnetization curves recorded at different temperatures. The solid lines are the ab initio simulations. (b) Magnetization and reduced magnetization curves for **2** at 2 (blue), 5 (gray), and 8 K (red). Solid lines are the ab initio simulations.

(a)

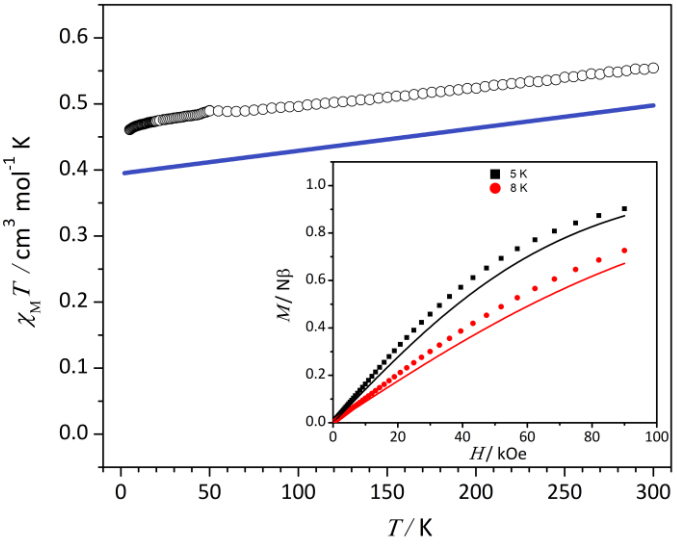

(b)

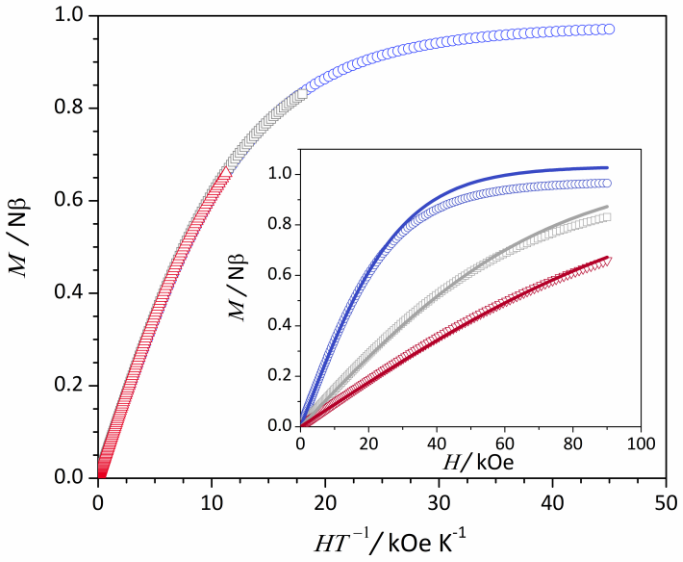

Figure S8. (a) Diagram showing the splitting of the five 4d orbitals on the Ru1 anion unit in **1**. The energy scale is taken from the CASSCF calculation. (b) Model of this anion in **1** with its principal magnetization axes represented by arrows.

(a)

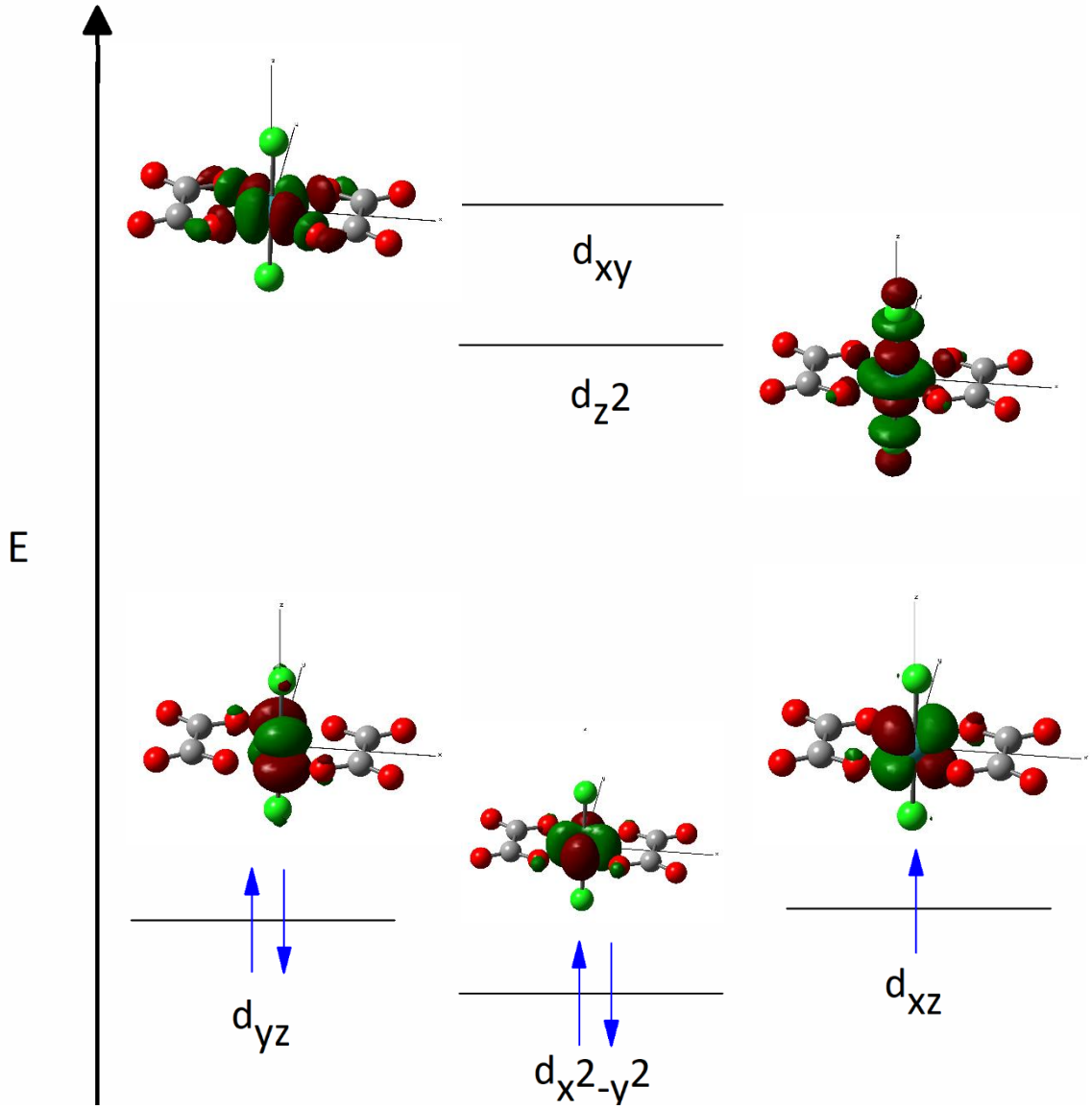

(b)

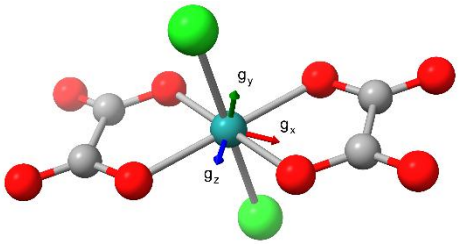

Figure S9. Thermal dependence of $\chi_M T$ for **3** measured under and applied field of 1.0 kOe. Inset: Reduced magnetization curves recorded at 2 (blue), 5 (gray), and 8 K (red).

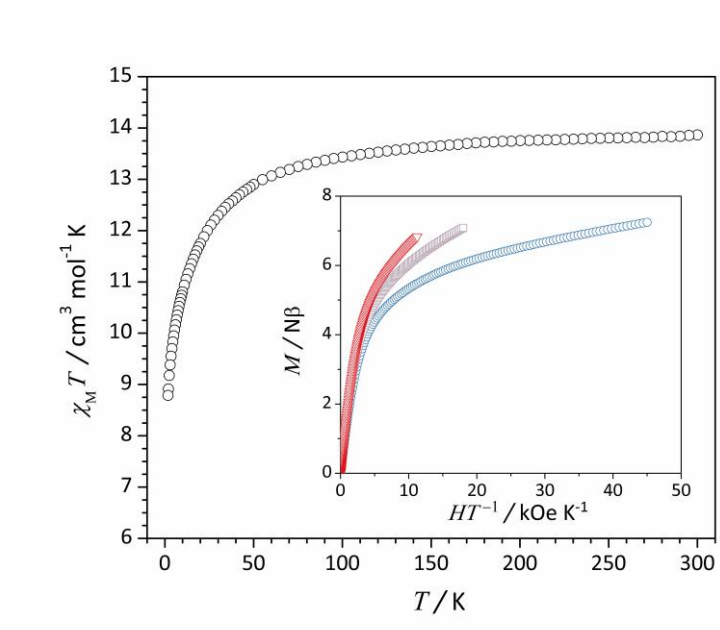

Figure S10. Frequency dependence of χ_M' and χ_M" at different temperatures for **1** under an external dc field of 1.0 (top) and 2.0 kOe (bottom). The solid curves are theoretical calculations based on the generalized Debye model.[6] Temperature points for which a maximum in χ_M" is not observed were discarded.

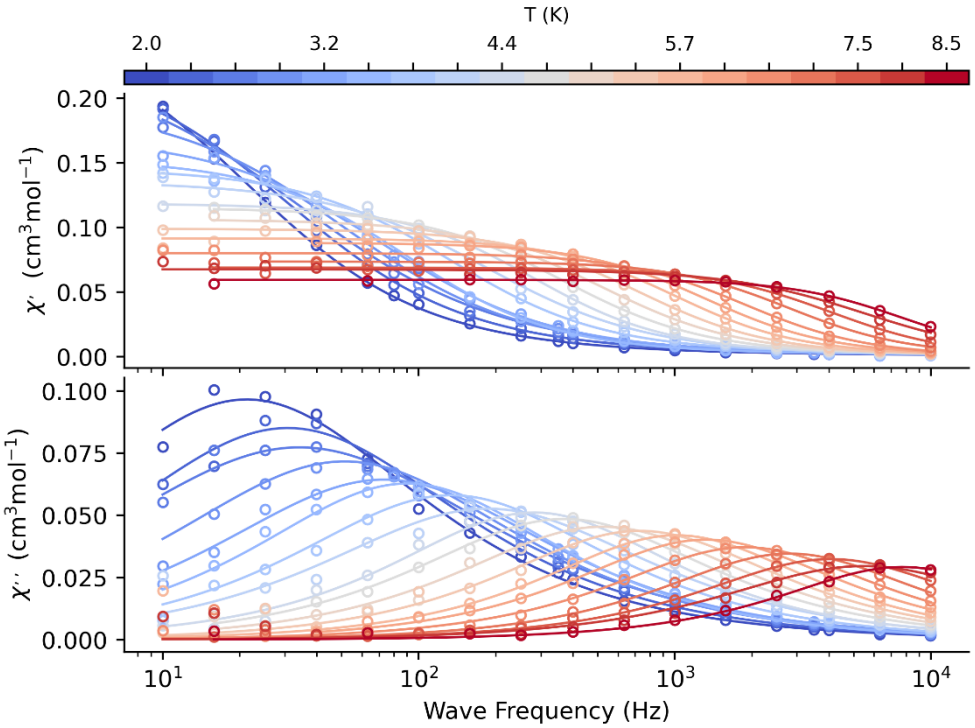

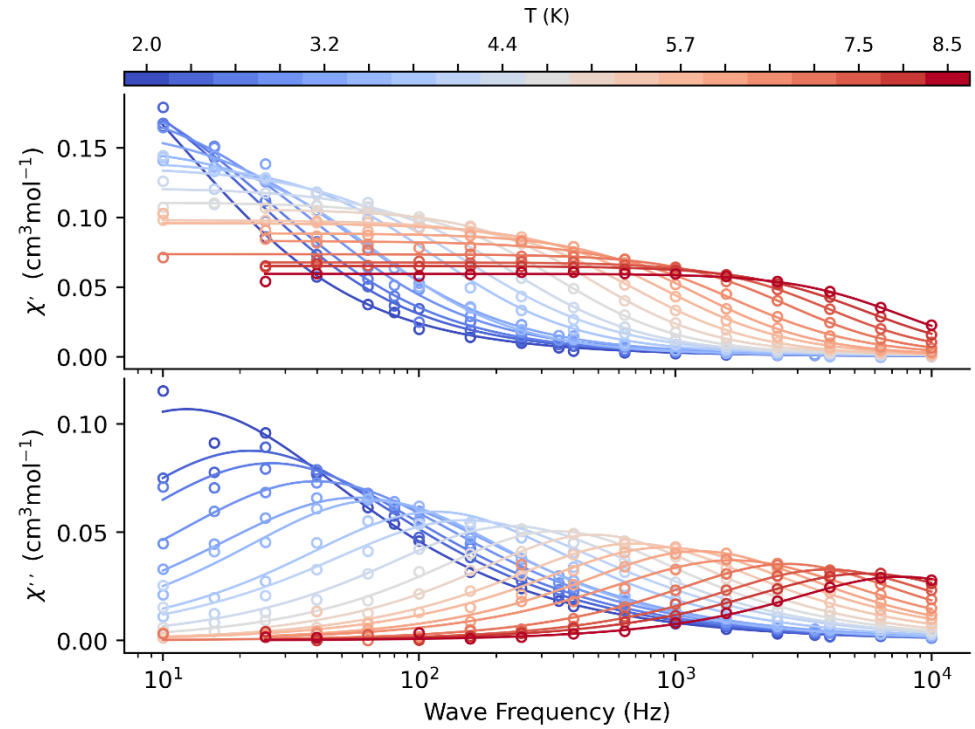

Figure S11. Argand diagram of **1** between 2.0 K (blue) and 8.5 K (red) under a dc field of 1.0 (top) and 2.0 kOe (bottom).[7] Lines represent the best fits as calculated with the generalized Debye model.

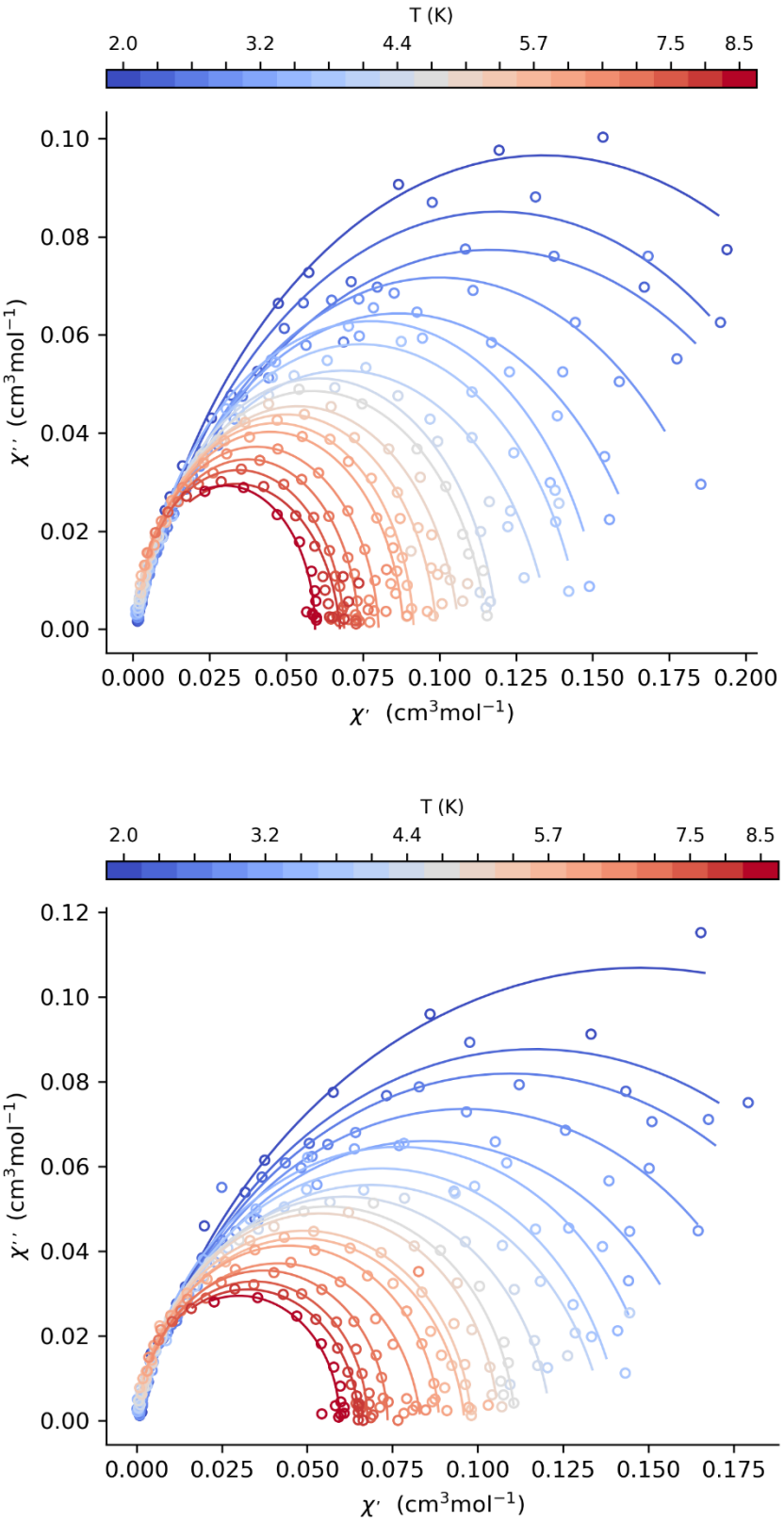

Figure S12. Frequency dependence of χ_M' and χ_M'' at different temperatures for **2** under an external dc field of 2.0 kOe (top) and related Argand diagram (bottom). The solid curves are theoretical calculations based on the generalized Debye model.

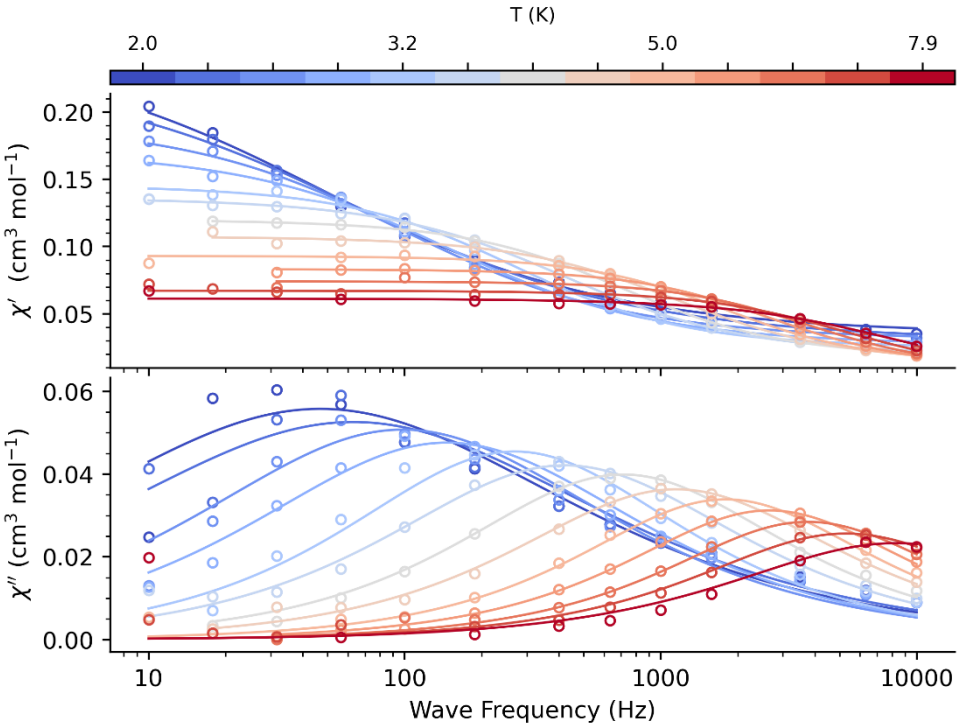

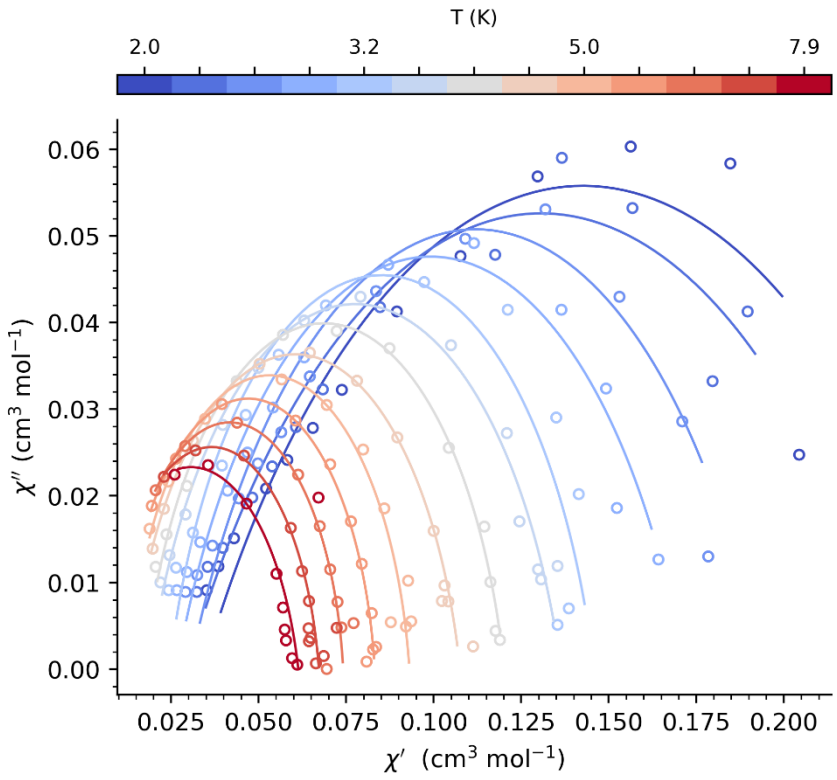

Figure S13. Frequency dependence of χ_M' and χ_M'' under different dc fields for **1** (top) and **2** (bottom) at 2.0 K. The solid curves are theoretical calculations based on the generalized Debye model.[6]

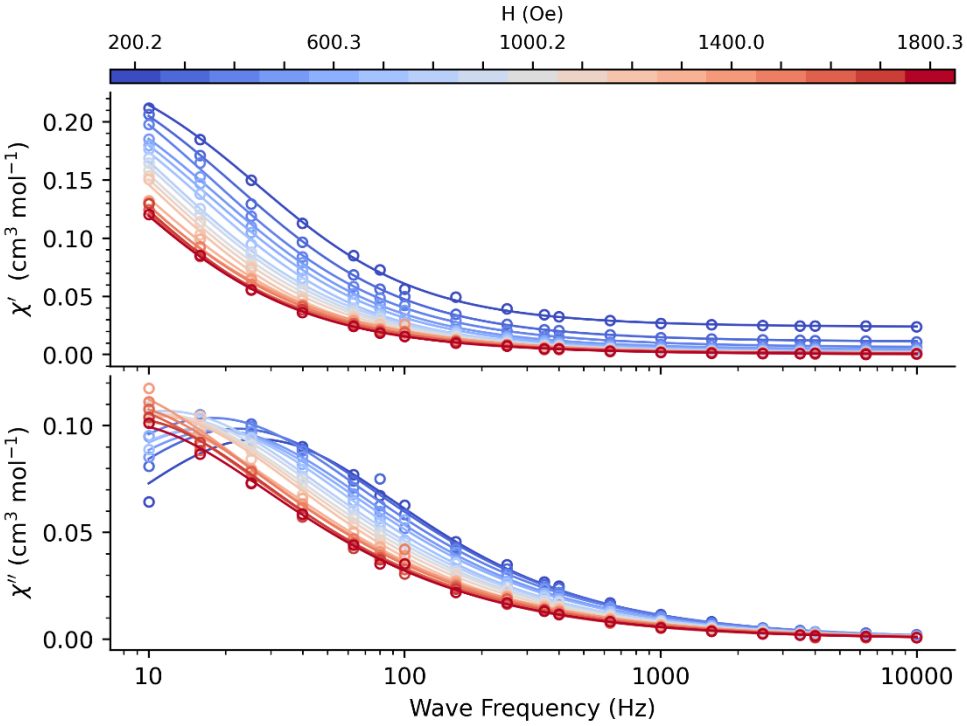

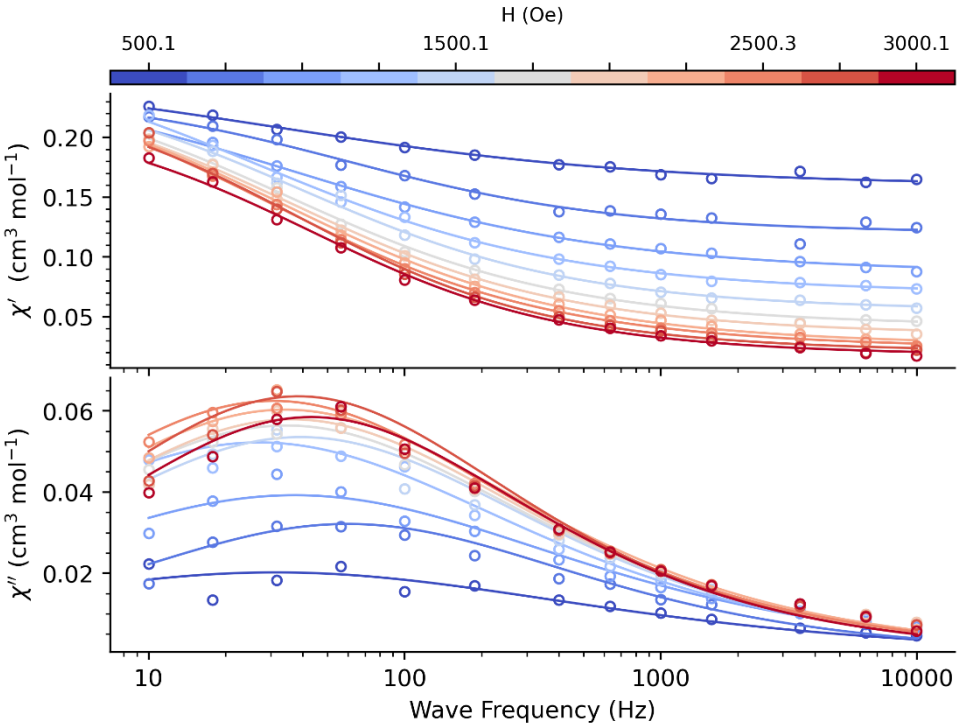

Figure S14. Temperature dependence of the relaxation-time distribution width, α, for **1** under applied dc fields of 1.0 (green) and 2.0 kOe (red) and for **2** under 2.0 kOe (blue) (top). Dc-field dependence of α for **1** (black) and **2** (red) at 2.0 K (bottom). Error bars were calculated using the log-normal distribution model at the 1σ level implemented in the CC-Fit2 software. Lines serve only as a visual guide.

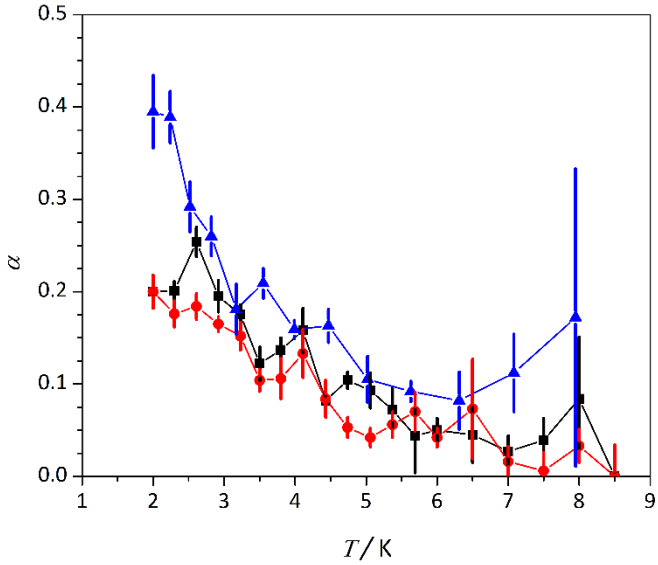

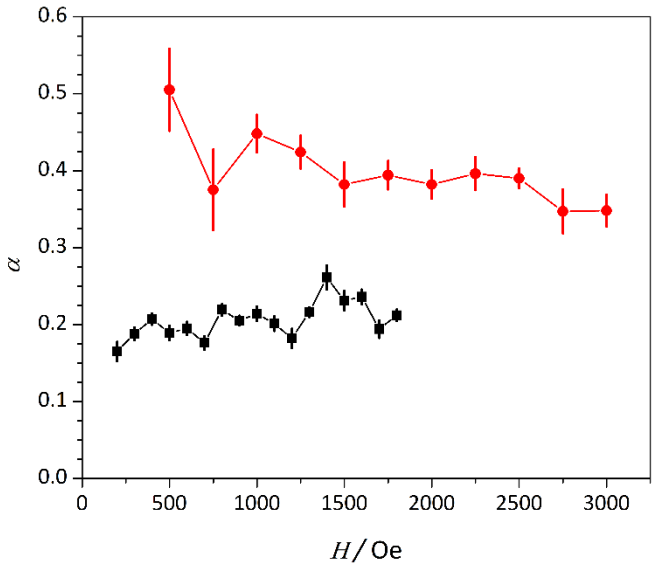

Figure S15. Dc-Field dependence of the relaxation rate for **1** (top) and **2** (bottom) at 2.0 K. Error bars were calculated using the log-normal distribution model at the 1σ level implemented in the CC-Fit2 software. Red lines are guides to the eye.

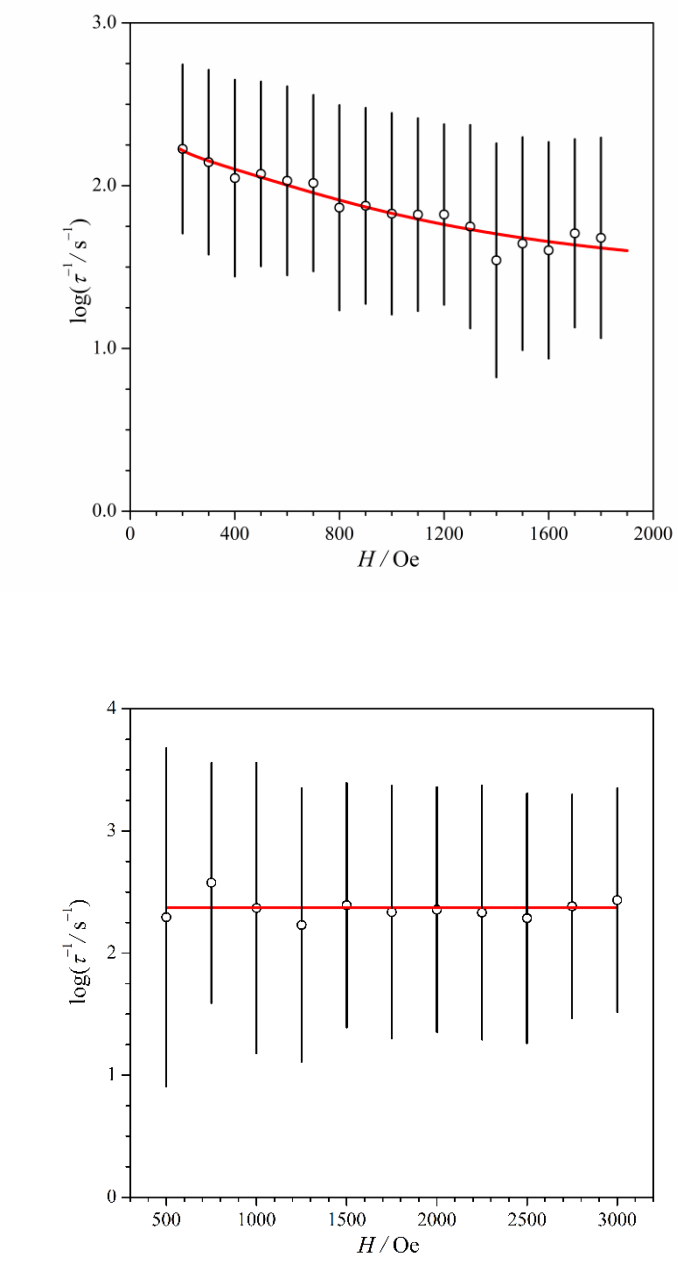

Figure S16. Temperature dependence of the relaxation rate for **1** (top) and **2** (bottom) under an external field of 1.0 and 2.0 kOe, respectively. Error bars were calculated using the log-normal distribution model at the 1σ level implemented in the CC-Fit2 software. Solid lines are the best fits for a Raman decay process (**2**) or a Raman + direct process (**1**).

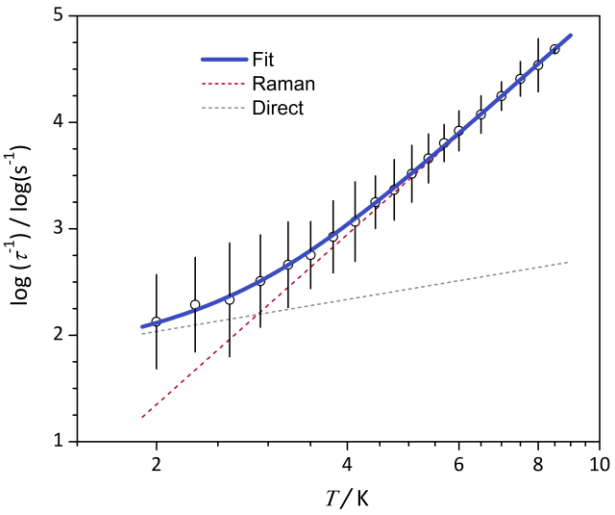

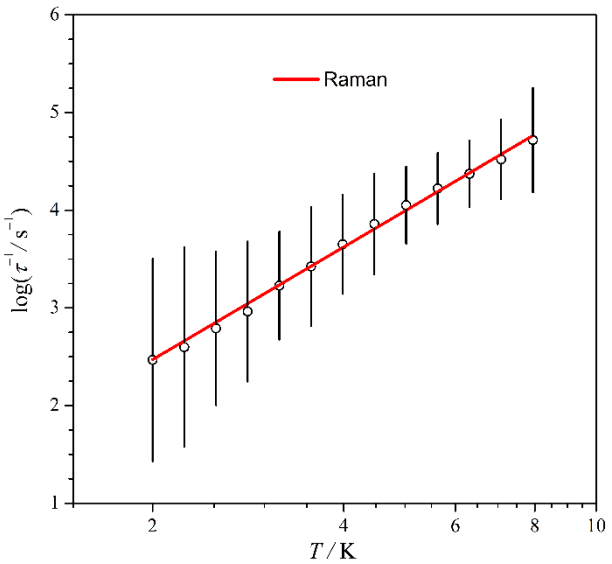

References.

1 CrysAlisPro Software system, 1.171.39.46, Rigaku Corporation, Oxford, UK, 2018.
2 G. M. Sheldrick, *Acta Cryst A*, 2015, **71**, 3–8.
3 G. M. Sheldrick, *Acta crystallographica. Section C, Structural chemistry*, 2015, **71**, 3–8.
4 O. V. Dolomanov, L. J. Bourhis, R. J. Gildea, J. a. K. Howard and H. Puschmann, *J Appl Cryst*, 2009, **42**, 339–341.
5 D. Reta and N. F. Chilton, *Phys. Chem. Chem. Phys.*, 2019, **21**, 23567–23575.
6 D. Gatteschi, R. Sessoli and J. Villain, *Molecular Nanomagnets*, Oxford University Press, 2006.
7 K. S. Cole and R. H. Cole, *The Journal of Chemical Physics*, 1941, **9**, 341–351.
8 F. Neese, *WIREs Computational Molecular Science*, 2012, **2**, 73–78.
9 L. F. Chibotaru and L. Ungur, *J. Chem. Phys.*, 2012, **137**, 064112.
10 F. Weigend and R. Ahlrichs, *Phys. Chem. Chem. Phys.*, 2005, **7**, 3297–3305.
11 F. Weigend, *J Comput Chem*, 2008, **29**, 167–175.
12 C. Angeli, R. Cimiraglia, S. Evangelisti, T. Leininger and J.-P. Malrieu, *J. Chem. Phys.*, 2001, **114**, 10252–10264.
13 A. Panja, S. Paul, E. Moreno-Pineda, R. Herchel, N. Ch. Jana, P. Brandão, G. Novitchi and W. Wernsdorfer, *Dalton Transactions*, 2024, **53**, 2501–2511.
14 M. Douglas and N. M. Kroll, *Annals of Physics*, 1974, **82**, 89–155.
15 D. Aravena, F. Neese and D. A. Pantazis, *J. Chem. Theory Comput.*, 2016, **12**, 1148–1156.
16 J. D. Rolfes, F. Neese and D. A. Pantazis, *Journal of Computational Chemistry*, 2020, **41**, 1842–1849.
17 F. Weigend, *Phys. Chem. Chem. Phys.*, 2006, **8**, 1057–1065.
18 F. Neese, F. Wennmohs, A. Hansen and U. Becker, *Chemical Physics*, 2009, **356**, 98–109.
19 C. Adamo and V. Barone, *J. Chem. Phys.*, 1999, **110**, 6158–6170.
20 A. D. Becke, *J. Chem. Phys.*, 1993, **98**, 5648–5652.
21 T. Yanai, D. P. Tew and N. C. Handy, *Chemical Physics Letters*, 2004, **393**, 51–57.
22 V. N. Staroverov, G. E. Scuseria, J. Tao and J. P. Perdew, *J. Chem. Phys.*, 2003, **119**, 12129–12137.
23 Y. Zhao and D. G. Truhlar, *Theor Chem Account*, 2008, **120**, 215–241.
24 N. Mardirossian and M. Head-Gordon, *J. Chem. Phys.*, 2016, **144**, 214110.
25 E. Caldeweyher, S. Ehlert, A. Hansen, H. Neugebauer, S. Spicher, C. Bannwarth and S. Grimme, *J. Chem. Phys.*, 2019, **150**, 154122.
26 S. Grimme, S. Ehrlich and L. Goerigk, *Journal of Computational Chemistry*, 2011, **32**, 1456–1465.
27 K. Yamaguchi, Y. Takahara and T. Fueno, in *Applied Quantum Chemistry*, eds. V. H. Smith, H. F. Schaefer and K. Morokuma, Springer Netherlands, Dordrecht, 1986, pp. 155–184.
28 M. E. Lines, *J. Chem. Phys.*, 1971, **55**, 2977–2984.
29 A. Ruiz-Martínez, D. Casanova and S. Alvarez, *Dalton Trans.*, 2008, 2583–2591.
30 D. Casanova, M. Llunell, P. Alemany and S. Alvarez, *Chemistry – A European Journal*, 2005, **11**, 1479–1494.